

Understanding NMR relaxometry of partially water-saturated rocks

O. Mohnke, R. Jorand, C. Nordlund, N. Klitzsch

Institute for Applied Geophysics and Geothermal Energy (GGE), E.ON Energy Research Center (E.ON ERC), RWTH Aachen University, Mathieustrasse 10, 52074 Aachen

Abstract

Nuclear Magnetic Resonance (NMR) relaxometry measurements are commonly used to characterize the storage and transport properties of water-saturated rocks. These assessments are based on the proportionality of NMR initial signal amplitude and relaxation time to porosity (water content) and pore size, respectively. ~~Herein, The relationship between pore size and NMR relaxation time depends on~~ pore shapes, ~~which is~~ are usually assumed to be spherical or cylindrical. However, the NMR response at partial water saturation for natural sediments and rocks may differs strongly from the responses calculated for spherical or cylindrical pores, because these pore shapes cannot account for water menisci remaining in the corners of de-saturated angular pores. Therefore, we consider a bundle of pores with triangular cross-sections. We introduce analytical solutions of the NMR equations at partial saturation of these pores, which account for water menisci of de-saturated pores. After developing equations that describe the water distribution inside the pores, we calculate the NMR response at partial saturation for imbibition and drainage based on the deduced water distributions.

For this pore model, NMR amplitude and NMR relaxation time at partial water saturation strongly depend on pore shape even so the NMR relaxation time at full saturation only depends on the surface to volume ratio of the pore. The pore-shape-dependence at partial saturation arises from the pore shape and capillary pressure dependent water distribution in pores with triangular cross-sections. Moreover, we show the qualitative agreement of the

26 saturation dependent relaxation time distributions of our model with those observed for rocks
27 and soils.

28 1 Introduction

29 Understanding multi-phase flow processes in porous rocks and soils is vital for addressing
30 a number of problems in ~~the~~ geosciences such as oil and gas recovery or vadose zone
31 processes, which influence groundwater recharge and evaporation. Effective permeability,
32 which is defined as the permeability of a fluid in presence of another fluid, is the decisive
33 parameter for fluid transport, and depends on fluid saturation, wetting condition, and pore
34 structure. In addition, saturation history influences the fluid content and the effective
35 permeability (for a specific pressure), which are different for imbibition and drainage.

36 A method considered suitable for determining water content of rocks non-invasively is
37 nuclear magnetic resonance (NMR), because the NMR initial signal amplitudes are directly
38 proportional to the hydrogen content in the pore space, and the NMR relaxation times are
39 linked to the size of the water-containing pores in the rock. In a two-phase system of water
40 and air only the water contributes to the NMR signal response. Therefore, NMR is widely
41 used for estimating transport and storage properties of rocks and sediments (Kenyon, 1997;
42 Seevers 1966; Fleury et al., 2001; Arnold et al., 2006).

43 In recent years, several researchers have studied the relationship between NMR and
44 multiphase flow behavior on the pore scale to better understand and infer the storage and
45 transport properties of partially saturated rocks or sediments (e.g., Chen et al., 1994; Liaw et
46 al. 1996; Ioannidis et al., 2006; Jia et al., 2007; Al-Mahrooqi et al., 2006; Costabel and
47 Yaramanci, 2011, 2013; Talabi et al., 2009). As an extension of this research, we study the
48 relationship between the water distribution inside the pores of a partially saturated rock and
49 the system's NMR response by using bundles of pore with triangular cross-sections. While
50 Al-Mahrooqi et al. (2006) used a similar modeling approach to infer the wettability properties
51 in oil-water systems, this study investigates the evolution of the NMR relaxation-time spectra
52 during drainage and imbibition. For this purpose, we consider a capillary pore ensemble that

is partially saturated with water and air. Traditionally, the pores within this ensemble are assumed to have a cylindrical geometry. Depending on pressure, cylindrical capillaries are either water- or air-filled and thus they either contribute to an NMR response or they do not. Consequently, the NMR relaxation times of partially water-saturated capillary pore bundles always remain subsets of the fully saturated system's relaxation-time distribution, i.e., they are a function inside the envelope of the distribution curve at full saturation (see Fig. 1-a). However, in porous rocks, which are formed by the aggregation of grains, the pore geometry is usually more complex (Lenormand et al., 1983; Ransohoff and Radke, 1987; Dong and Chatzis, 1995) and may exhibit angular and slit-shaped pore cross-sections rather than cylindrical capillaries or spheres (Fig. 2a). For example, in tight gas reservoir rocks Desbois et al. (2011) found three types of pore shapes that are controlled by the organization of clay sheet aggregates: i) elongated or slit-shaped, ii) triangular, and iii) multi-angular cross-sections. The relaxation-time distribution functions derived from NMR measurements for such partially saturated rocks are frequently found to be shifted towards shorter relaxation times outside the original envelope observed for a fully saturated sample, (Fig. 2b) (e.g., Applied Reservoir Technology Ltd., 1996; [Bird et al., 2005](#); [Jaeger et al., 2009](#); Jorand et al., 2010; Stingaciu, 2010a,b; [Costabel, 2011](#)). In angular pores, water will remain trapped inside the pore corners even if the gas entry pressure is exceeded. Standard NMR pore models that assume cylindrical or spherical pore ensembles (e.g., Kenyon, 1997), however, do not account for such residual water (Blunt et al., 2002; Tuller et al., 1999; Or and Tuller, 2000; Tuller and Or, 2001; [Thern, 2014](#)). To overcome this limitation, we [adopt an NMR modeling approach initially proposed and discussed by Costabel \(2011\) and present](#) numerical simulations and analytical solutions of the NMR equations for partially saturated pores with triangular cross-sections to quantify NMR signal amplitudes and relaxation times. The NMR response of a triangular capillary

during drainage and imbibition depends on the water distribution inside the capillary, which is subject to pore shape and capillary pressure. Thus, in the next chapter we present the relationship between capillary pressure and water distribution inside cylindrical and triangular pore geometries during drainage and imbibition. For this purpose, the reduced similar geometry concept introduced by Mason and Marrow (1991) is used. Subsequently, based on the spatial water distribution, an analytical solution of the NMR diffusion equation (Torrey, 1956; Brownstein and Tarr, 1979) for partially saturated triangular capillaries is derived and tested by numerical simulations (Mohnke and Klitzsch, 2010). The derived equations are used to study the influence of pore size distribution and pore shape of triangular capillaries on the NMR response, in particular considering the effects of trapped water. Finally, an approach for simulating NMR signals during imbibition and drainage of triangular pore capillaries is introduced and demonstrated -using synthetic pore size distributions.

2 Results and discussion

2.1 Water distribution during drainage and imbibition in a partially saturated triangular tube

In a partially saturated pore space, a curved liquid-vapor interface called the arc meniscus (AM) arises due to the pore's capillary forces. In addition, adsorptive forces between water and matrix lead to the formation of a thin water film at the rock-air interface. Such water films with a thickness typically below 20 nm (e.g., Toledo et al., 1990; Tokunaga and Wan, 1997) exhibit very short NMR relaxation times. Although water films to some extent may influence transport properties and water distribution of a partially saturated porous system (Tuller and Or, 2001), the contribution of the film volume to NMR amplitudes is very small with respect to the NMR signal amplitudes arising from the water trapped in the menisci, i.e., $V_{\text{film}} \ll V_{\text{meniscus}}$. Therefore, for sake of simplicity, we neglect water films in his study.

103 In the following discussion, we consider a triangular capillary, initially filled with a
 104 perfectly wetting liquid, i.e., contact angle $\theta = 0^\circ$, which exhibits a constant interfacial
 105 tension σ ($\sigma_{\text{air-water}} = 73 \times 10^{-3} \text{ Nm}^{-1}$ at 20°C) and is under the assumption that gravity
 106 forces are weak and therefore can be neglected. The two-phase capillary entry pressure as
 107 derived by the MS-P method (Mayer and Stowe, 1965; Princen, 1969a, b, 1970) can be
 108 expressed by the Young-Laplace equation:

$$p_c = \frac{\sigma \cos \theta}{r_{\text{AM}}} = \frac{\sigma}{r_{\text{AM}}}, \quad (1)$$

109 where r_{AM} is the radius of the interface arc meniscus and p_c is the minimum pressure
 110 difference necessary for a non-wetting fluid-phase, i.e., air, to invade a uniformly wetted (tri-)
 111 angular tube filled with a denser phase, i.e., water (see Fig. 3a). Upon consideration of a
 112 pressure difference $p > p_c$, the non-wetting fluid-phase will begin to enter the pore and
 113 occupy the central portion of the triangle, whereas – separated by the three interface arc
 114 menisci of radius r_{AM} – the wetting fluid remains in the pore corners (Fig. 3a).

115 From an original triangle ABC , a new smaller triangle $A'B'C'$ of similar geometry with an
 116 inscribed circle of radius $r' = r_{\text{AM}} < R_0$ can be constructed by means of the reduced similar
 117 geometry concept as introduced by Mason and Morrow (1991) (Fig. 3b). To account for
 118 different transport mechanisms during imbibition and drainage of the denser wetting phase,
 119 Mason and Morrow (1991) introduced two different principal displacement curvatures with
 120 radii r_I and r_D , respectively.

121 During imbibition of a (tri-)angular pore, the radius of curvature r_{AM} increases until the
 122 separate arc menisci of the corners touch and the pore fills spontaneously (“snap off”). The
 123 critical radius of curvature r_I , which is equal to the radius of the pore’s inscribing circle, for
 124 the angular pore at “snap-off” pressure p_I is then given by

$$r_I = \frac{2A}{P}, \quad (2)$$

125

126 According to Eq. 2, the snap-off pressure depends on the geometry of the triangle only,
127 i.e., on its cross-sectional area A and perimeter P . In contrast, during drainage the threshold
128 radius of curvature $r_D = r_{AM}$, at which the center of the fully saturated angular capillary
129 spontaneously empties as a non-wetting fluid phase invades the pore, is given by

$$r_D = P \left[\frac{1}{2G} + \left(\frac{\pi}{G} \right)^{1/2} \right]^{-1}, \quad (3)$$

130 with $r_D < r_l$ and drainage threshold pressure $p_D > p_l$. The dimensionless and size-
131 independent factor $G = \frac{A}{P^2} \left(= \frac{A'}{P'^2} \right)$ reflects the shape of the triangle depending on its cross-
132 sectional area A and perimeter P (A' and P' refer to the reduced triangle), i.e., from near-slit-
133 shape ($\lim_{\gamma \rightarrow 0} G = 0$) to equilateral shape ($G = 0.048$). A detailed derivation of Eqs. 2 and 3
134 as a consequence of hysteresis between drainage and imbibition can be found in Mason and
135 Morrow (1991).

136 Note, that the permeability of a porous system of such triangular capillaries is strongly
137 influenced by the shape factor G . For single-phase laminar flow in a triangular tube the
138 hydraulic conductance g is given by the Hagen-Poiseuille formula

$$g = k \frac{A^2 G}{\mu} \quad (4)$$

139 with the cross-sectional area A , the shape factor G , the fluid viscosity μ , and k being a
140 constant accounting for the geometrical shape of the cross-section, e.g. $k = 0.5$ for circular
141 tubes and $k = 0.6$ for a tube with a cross-section of an equilateral triangle (Patzek and Silin,
142 2001). The hydraulic conductance of an irregular triangle is closely approximated by
143 equation 1 using the same constant k as for an equilateral triangle (Øren et al., 1998). Thus,

for a constant cross-sectional area the hydraulic conductance g of the pore is proportional to its shape factor G .

Combining Eqs. 1–3 with the concept of reduced similar geometry discussed above, the degree of water saturation (S_w) inside a single triangular tube with cross-sectional area A_0 , perimeter P_0 , and radius R_0 of its inscribing circle at a given capillary pressure p_c during imbibition and drainage can be calculated according to

$$S_w^I(p, A_0, P_0) = \begin{cases} 1 & , p_c \leq p_I \quad (R_0 \leq r_I) \\ \frac{A_\Delta(p_c)}{A_0} & , p_c > p_I \quad (R_0 > r_I) \end{cases} \quad (\text{imbibition}) \quad (5)$$

$$S_w^D(p_c, A_0, P_0) = \begin{cases} 1 & , p_c < p_D \quad (R_0 < r_D) \\ \frac{A_\Delta(p_c)}{A_0} & , p_c \geq p_D \quad (R_0 \geq r_D) \end{cases} \quad (\text{drainage}) \quad (6)$$

The total area A_Δ of the triangular tube's water retaining corners, $\gamma_{1,2,3}$ (i.e., the gray areas in Figs. 4 and 5) is expressed by

$$A_\Delta(p_c) = \sum_{i=1}^3 A_{\gamma_i}(p_c), \quad (7a)$$

where

$$A_{\gamma_i}(p_c) = \left(\frac{1}{\tan \frac{\gamma_i}{2}} - \frac{(\pi - \gamma_i)}{2} \right) r_{AM}^2(p_c), \quad 0 < \gamma_i < \pi \quad (7b)$$

is the area of the triangle's i th water-filled corner (Tuller and Or, 1999). Consequently, the total effective area A_Δ still occupied by water is equal to the difference between the (reduced) triangular pore area \tilde{A} and the area πr_{AM}^2 of its respective inscribing circle (see Fig. 3). Above

159 equations can be simplified to $A_{\Delta} = (3\sqrt{3} - \pi) r_{AM}^2(p_c)$ when considering equilateral
 160 triangles, i.e., $\gamma_{1,2,3} = \frac{\pi}{3}$. The radius $r_{AM}(p_c)$ of the reduced triangle's arc meniscus can be
 161 directly calculated from Eq. 1. Calculated pressure-dependent water and gas distributions
 162 during imbibition and drainage for an equilateral and arbitrary triangular capillary are shown
 163 in Figs. 4a and 5a. The corresponding water retention curves plotted in Figs. 4b and 5b
 164 illustrate the resulting hysteresis behavior of the partially saturated system and can be
 165 subdivided into three parts: at low capillary pressures, i.e., $p_c < p_l$, the pore always remains
 166 fully water-saturated. For the interval $p_l < p_c \leq p_D$, two separate behaviors are observed:
 167 during imbibition, the water content gradually increases with increasing capillary pressure,
 168 while during drainage the pore still remains fully saturated. For pressure levels $p_c \geq p_D$, both
 169 drainage as well as imbibition exhibit the same gradual decrease of water saturation.

170 In the following section, analytical solutions for respective NMR responses that arise
 171 from partially saturated arbitrary triangular tubes are derived and validated with numerical
 172 simulations of the NMR diffusion equations.

173

174 2.2 NMR response for triangular capillaries

175 NMR relaxometry is commonly employed for petrophysical investigations of saturated
 176 porous rocks in well-logging and laboratory studies. In this respect, the NMR method is a
 177 unique geophysical tool, which delivers direct information about the water content and allows
 178 to infer the pore-size distribution in rock samples or the subsurface. The measured NMR
 179 relaxation signal $M(t)$ is constituted by superposition of all signal-contributing pores in a rock
 180 sample (e.g., Coates et al., 1999; Dunn et al., 2002):

$$\frac{M(t)}{M_0} = \frac{1}{V_0} \sum_i^N \left(v_i \times \left(1 - e^{t \cdot T_{i,1}^{-1}} \right) \right), \quad (8)$$

181 where M_0 and V_0 are the equilibrium magnetization and total volume of the pore system,
182 respectively. The saturated volume of the i th pore and its corresponding longitudinal
183 relaxation constant are given by v_i and T_{i1} , respectively.

184 Following derivations of Brownstein and Tarr (1979), the inverse of the longitudinal
185 relaxation time T_1 is linearly proportional to the surface-to-volume ratio of a pore according
186 to

$$T_1^{-1} = T_{1B}^{-1} + \rho_s \frac{S_a}{V}, \quad (9)$$

187 where T_{1B} is the bulk relaxation time of the free fluid and ρ_s is the surface relaxivity, a
188 measure of how quickly protons ~~lose orientation or phase coherence their magnetization~~ due
189 to magnetic interactions at the fluid-solid interface, which can be attributed to paramagnetic
190 ions at mineral grain surfaces. V and S_a are the pore's volume and active surface boundaries,
191 respectively. In this context, an active boundary refers to an interfacial area, i.e., the pore
192 wall, where $\rho > 0$ and, thus, enhanced NMR relaxation will occur as the molecules diffuse ~~to~~
193 at the pore walls. This model, however, is based on the general assumption of a relaxation
194 regime that is dominated by surface relaxation processes (*fast diffusion*), i.e., the fluid
195 molecules move sufficiently fast and thus explore all parts of the pore volume with respect to
196 the time scale ($\sim T_1$) of the experiment.

197 Upon consideration of a long (triangular) capillary, its surface-to-volume-ratio equals its
198 perimeter-to-cross-section-ratio, i.e., $S/V = P/A$. Consequently, Eq. 9 can be written as

$$T_1^{-1} = T_{1B}^{-1} + \rho \frac{P_0}{A_0}, \quad (10)$$

199 where P_0 is the saturated tube's (active) perimeter and A_0 its cross-sectional area for a circular
200 cross-section, $\frac{P_0}{A_0} = \frac{2}{r_0}$, with r_0 being the capillary radius. Hence, the relaxation rate of a fully
201 saturated arbitrary triangular pore ABC can be expressed in terms of its shape factor G and
202 perimeter P_0 :

Formatted: Font: Italic

$$T_1^{-1} = T_{1B}^{-1} + \frac{\rho}{G P_0} \left(= T_{1B}^{-1} + \rho \frac{L_{AB} + L_{BC} + L_{CA}}{L_{AB} L_{CA} \sin(\gamma_A)} \right) , \quad (11)$$

where L_{AB} , L_{BC} , and L_{AC} are the lengths of a triangle's sides and γ_A is the angle at corner A (see Fig. 3). As illustrated in Fig. 6, the relaxation times of a fully saturated pore decrease with decreasing pore shape factor G – and thus, decreasing hydraulic conductance – and increasing pore perimeter P . By reducing one angle from 60° to 0° while fixing another at 60° , we increase P/A for a constant cross-sectional area A . In the special case of an equilateral triangular capillary, i.e., $P_0/A_0 = \frac{12}{\sqrt{3} L_0}$, Eq. 11 can be simplified to

$$T_1^{-1} = T_{1B}^{-1} + \rho \frac{12}{\sqrt{3} L_0} . \quad (12)$$

Now we consider the previously discussed water-air system of a partially saturated equilateral triangular capillary. Here, the NMR signal will originate from the water retained at the corners. Replacing A_0 in Eq. 10 with an effective area A_γ or A_Δ as derived by Eqs. (7a) and b, respectively. A_Δ reflects the actual pore fraction that contributes to the NMR signal, i.e., the portion of the pore area A_0 that still remains occupied by water.

Supposing the air-water interface to be a passive boundary with respect to NMR surface relaxivity, i.e., $\rho = 0$, the effective active boundary is exclusively controlled by the pore wall segments ($\rho > 0$) in contact with water (wetting phase) (Fig. 7). Thus, the active perimeter of such a partially saturated triangular capillary is equal to its pressure-dependent reduced triangle's perimeter, $P'_\Delta(r^{L,D}(p_c))$, according to

$$P_\Delta = \sum_{i=1}^{N=3} P_{\gamma_i} , \quad (13)$$

with

Formatted: Font: Not Italic

Formatted: Font: Not Italic

Formatted: Font: Italic

$$P_{\gamma_i} = 2 \frac{r_{AM}(p_c)}{\tan \frac{\gamma_i}{2}}, \quad 0 < \gamma_i < \pi \quad (14)$$

being the perimeter of the i th water-filled corner. Consequently, the NMR relaxation rates and NMR signal (amplitude) evolution during drainage and imbibition of a single equilateral triangular capillary can be expressed by

$$T_{\Delta,1}^{-1} = \begin{cases} T_{1B}^{-1} + \rho \frac{P_0}{A_0}, & S_w^{I,D} = 1 \\ T_{1B}^{-1} + \rho \frac{P_{\Delta}^{I,D}(p_c, A_0, P_0)}{A_{\Delta}^{I,D}(p_c, A_0, P_0)}, & S_w^{I,D} < 1 \end{cases} \quad (15)$$

and

$$\frac{m(t)}{m_0} = S_w^{I,D}(p_c, A_0, P_0) \left(1 - e^{\frac{-t}{T_{\Delta,1}}} \right), \quad (16)$$

respectively. Illustrated in Fig. 8 is the pressure-dependent water distribution inside a single equilateral triangular capillary (with a side length of $1 \mu\text{m}$) during drainage (a) and corresponding evolution of longitudinal magnetization (b). As the water saturation is reduced with increasing pressure, both NMR amplitudes and relaxation times (c) decrease. Note that only a single characteristic relaxation time at each saturation degree is observed, since each corner has the same P_{γ}/A_{γ} , and consequently the same T_1 value.

In contrast, each water-filled corner of a partially saturated non-equilateral triangle, i.e., $\gamma_1 \neq \gamma_2 \neq \gamma_3$, can have a different P_{γ}/A_{γ} ratio, and thus will show a different relaxation time and amplitude. As a result, depending on its individual shape, even a single partially saturated pore exhibits a multi-exponential NMR relaxation behavior based on Eq. (8) according to

$$\frac{m(t)}{m_0} = \frac{1}{A_0} \sum_{i=1}^{N=3} A_{\gamma_i}^{I,D} \left(1 - e^{\frac{-t}{T_{\gamma_i,1}}} \right), \quad (17)$$

236 with $T_{Y_{i,1}} = \frac{1}{T_{1B}} + \rho \frac{P_{Y_i}}{A_{Y_i}}$ and $\frac{A_{Y_i}^{1,D}}{A_0}$ being the characteristic relaxation time and amplitude
 237 contribution of the i th corner of the triangle, respectively. Figure 9 exemplifies such different
 238 multi-exponential relaxation behavior for a pore with a right triangle geometry with angles of
 239 ($\gamma_1 = 30^\circ, \gamma_2 = 60^\circ, \gamma_3 = 90^\circ$) and the same cross-sectional area as the equilateral pores in
 240 Fig. 8 (i.e., \sim NMR porosity).

241 To test the analytical (fast diffusion) models for partially saturated triangular capillaries
 242 derived above, the calculated longitudinal NMR relaxation times and amplitudes are
 243 compared to solutions obtained from 2D numerical simulations of the general NMR diffusion
 244 equation (Mohnke and Klitzsch, 2010):

$$\dot{m} = \left(D \nabla^2 - \frac{1}{T_B} \right) m, \quad (18)$$

245 with normalized initial values $m(\mathbf{r}, t = 0) = \frac{M_0 - 1}{A}$ and boundary conditions

$$D \mathbf{n} \nabla m \Big|_P = \rho_s m \Big|_P, \quad (19)$$

246 where m is the magnetization density, D the diffusion coefficient of water, T_B the bulk
 247 relaxation time, ρ_s the interface's surface relaxivity, \mathbf{n} the outward normal, and A and P the
 248 pore's cross-sectional area and perimeter, respectively. The above equations were solved
 249 numerically using finite elements (Mohnke and Klitzsch, 2010) to simulate the respective
 250 NMR relaxation data of the studied triangular geometries.

251 As shown in Fig. 10, analytically (+) calculated NMR relaxation data for drainage and
 252 imbibition for an equilateral triangular pore are in a very good agreement ($R^2 > 0.99$) with
 253 data obtained from numerical simulations (o).

254 The model was also validated for pores with arbitrary angles. Figure 11 illustrates 2D
 255 finite elements simulations using saturated pore corners with angles γ_i ranging from 5° to
 256 175° with equal active surface-to-volume ratios $P_{Y_i} / A_{Y_i} = \text{const.}$ and thus $T_{1,i} = \text{const.}$ The

simulations were compiled and compared to their respective analytical solutions. The ratios of the numerical to the analytical model results for NMR amplitudes, i.e., NMR signal amplitudes, A_γ , and relaxation times, $T_{1,\gamma}$ as function of corner aperture γ are shown and confirm a near perfect correlation of $R^2 > 0.99$, with deviations generally less than 0.05 %. In this regard, the slight increase in divergence of relaxation time ratios at acute and obtuse angles can be attributed to numerical errors resulting from a decrease of the finite element's grid quality due to extremely high or low x-to-y ratios at these apertures. Note that the above model is applicable to any angular capillary geometry, such as square or octahedron.

2.3 Simulated water retention curves and NMR relaxation data of partially saturated pore distributions

The goal of this section is to evaluate how pore shape affects the forward-modeled NMR response of a partially saturated system of pores (a pore size distribution). As discussed earlier, the NMR relaxation time of a single water-filled capillary pore is inversely proportional to its surface-to-volume-ratio. Thus at full water saturation, the relaxation-time distribution obtained from a multi-exponential NMR relaxation signal represents the pore-size distribution of the rock. At partial water saturation, it is often assumed that the NMR relaxation signal still represents the pore size distribution of the water saturated pores (e.g., Stingaciu, 2010b), which we are going to show is true for the cylindrical but not for (tri-) angular pores.

In contrast to cylindrical pores, capillaries with (tri-)angular cross-sections may be partially water-saturated during drainage or imbibition (cf. Fig. 8 and 9) because of the water remaining in the corners. Thus, they show a different water retention behavior and the “desaturated” pores, i.e. their arc menisci, contribute to the NMR signal. Consequently, with increasing pressure (i.e. decreasing water saturation) the NMR relaxation behavior of the

partially water-saturated triangular capillary pore bundle successively shifts to signal contributions with shorter relaxation times reflecting the fast relaxation of residual water trapped in the pore corners (Figure 12). This behavior in angular pore geometries is demonstrated in Figure 13. Here, the NMR relaxation components for a fully (blue line) and partially saturated (red and green) distribution of triangular capillaries are plotted. The green and red peaks show the signals of the residual water in the pore corners. Following from the reduced geometry concept the remaining water in the corners has the same size and shape, i.e., the same NMR relaxation time, for all pores independent on their size but dependent on pressure. Therefore with decreasing saturation, i.e., increasing pressure, the NMR signal of the arc menisci increases and shifts towards smaller relaxation times. If the non-wetting phase (air) has entered all capillaries, only one single relaxation time remains for the pore bundle of equilateral triangles. For arbitrarily shaped triangular pores, three relaxation times would remain for the de-saturated pore system. Hence, the concept of a relaxation time distribution assumed in conventional NMR inversion and interpretation approaches would be no longer valid.

All the same, we apply the concept of fitting multi-exponential relaxation time distributions to NMR transients calculated for pore bundles of circular and equilateral triangle cross-sections to study how pore shape affects the typically-shown relaxation time distributions.

Water drainage and imbibition with water as wetting and air as non-wetting fluid were investigated by simulating water retention curves and corresponding NMR relaxation signals for a log-normal distributed pore size ensemble as shown in Figure 14.

Herein, to clarify the subsequent discussion we focused on the equilateral triangular capillary model. Note, that other angular pore shapes (e.g., right angular triangles or squares) will exhibit a similar behavior. Capillary pressure curves presented in Figure 15a were

calculated from -Eq. 1, 4, and 5 for pore bundles with circular and equilateral triangle cross-sections. In contrast to water retention curves calculated for the cylindrical capillary model significant hysteresis between drainage and imbibition can be observed for the triangular capillary model, i.e. in terms of initial amplitudes (=saturation) and respective mean relaxation times (Figure 15b). ~~presented water retention curves for drainage and imbibition were determined from the water distribution inside pores at a stationary states. Corresponding NMR T_1 relaxation -(saturation recovery) signals shown in Figure 15c, d and e were calculated using a uniform surface relaxivity of $\rho_s = 10 \mu\text{m/s}$ and water bulk relaxation $T_{1,bulk} = 3 s_2$~~

The NMR T_1 relaxation signals were simulated for 20 saturation levels of the drainage and imbibition curves ranging from $S = 100\%$ to $S < 1\%$ water saturation. The corresponding relaxation time distributions (Figure 15f-h) of the NMR T_1 transients were determined by means of a regularized multi-exponential fitting using a nonlinear least squares formulation solved by the Levenberg-Marquardt approach (e.g., Marquardt, 1963; Mohnke, 2010). Inverse modeling results of NMR data calculated for the drainage branches using the cylindrical capillary bundle (Fig. 15f) exhibit a shift of the distribution's maximum towards shorter relaxation times with decreasing saturation (i.e., increasing pressure). As anticipated, the derived distribution functions remain inside the envelope of the relaxation-time distribution curve at full saturation (see also Fig. 1a).

In contrast, inversion results for equilateral triangular capillary ensembles (Fig. 15f-h) – both for imbibition and drainage – show a similar shift to shorter relaxation times with decreasing saturation but also move outside the initial distribution at full saturation due to NMR signals originating from trapped water in the pore corners of the desaturated triangular capillaries. The effect of the pore corners on relaxation time at low saturations is also recognizable when comparing the (geometric) mean relaxation times, normalized to the

Formatted: Indent: First line: 0"

values observed at full saturation (Fig. 15b): Both, the drainage and the imbibition hysteresis branch of the triangular pore bundle show smaller mean relaxation times than the cylindrical pore bundle.

In conclusion, the calculated inverse models based for ~~on a~~ the triangular capillary bundle qualitatively agrees with the behavior of the inverted NMR relaxation-time distributions at partial saturation that are frequently observed in experimental data, e.g., of the Rotliegend sandstone shown in Fig. 2.

3 Summary and conclusions

Experimental NMR relaxometry data and corresponding relaxation-time distributions obtained at partial water/air saturation were explicated by a modification of conventional NMR pore models using triangular cross-sections. An analytical solution for calculating surface-dominated (fast diffusion) NMR relaxation signals in fully and partially saturated arbitrary angular capillaries ~~, while taking into account residual water trapped in pore corners,~~ was introduced and validated by numerical simulations.

Shape and size of triangular pores strongly influence both NMR and flow properties. The NMR relaxation time depends on the surface-to-volume ratio, which again depends on shape when considering angular pore capillaries. However, at partial saturation, the pore shape even more influences the water distribution inside the pore system, and thus the NMR signal. In contrast to cylindrical capillaries, angular capillaries also contribute to the NMR signal after desaturation of the pore due to water remaining in the corners.

In this regard, non-equilateral triangular capillaries at partial saturation exhibit a three-exponential relaxation behavior due to different perimeter-to-surface (= surface-to-volume) ratios of the water in the pore corners whereas the relaxation time of the trapped water in the corners depends on pressure (but not on pore size).

Furthermore, the shape and size of the triangular pores strongly influence both NMR and hydraulic properties. The NMR relaxation time depends on the surface-to-volume ratio (not on pore shape), while the water distribution inside the pore system, at partial saturation, is strongly influenced by the shape of the pore. Thus, the NMR signal at partial saturation is affected by not only the surface-to-volume ratio, but by the pore shape as well.

Moreover, we studied the NMR response of a triangular pore bundle model by jointly simulating water retention curves for drainage and imbibition and the corresponding NMR T_1 relaxometry data. With decreasing water saturation, the simulated NMR relaxation distributions shift towards shorter relaxation times below the initial distribution envelope at full saturation, which is principally in agreement with the relaxation behavior observed in experimental NMR data from rocks.

Ongoing research will include implementation of the introduced approach in an inverse modeling algorithm for NMR data obtained on partially saturated rocks to predict absolute and relative permeability at laboratory and borehole scales. Without considering angular pores the NMR signal of trapped water cannot be explained, i.e., using the classical approach of circular capillaries one cannot find a pore size distribution which explains the relaxation time distributions at all saturations sufficiently (e.g., Mohnke, 2014). On the other hand, angular pore models can account for the trapped water and thus overcome the limitation of the classical approach. Moreover, following the approach of Mohnke (2014) but considering angular pores we strive for estimating surface relaxivity, pore size distribution, and pore shape by jointly inverting NMR data at different saturations. Based on the obtained pore size distribution and triangle shape we expect to improve the prediction of the absolute and relative permeabilities considerably.

380 **Acknowledgements**

381 The study was supported by the German Research Foundation (DFG) in the framework of
382 the Transregional Collaborative Research Centre 32 (SFB TR 32) and Wintershall AG in the
383 framework of Wintershall Tight Gas Consortium at RWTH Aachen University.

384

385 **References**

- 386 Al-Mahrooqi, S. H., Grattoni, C. A., Muggeridge A. H., Zimmermann, R. W., and Jing, X.
387 D.: Pore-scale modelling of NMR relaxation for the characterization of wettability, J.
388 Petrol. Sci. Eng., 52, 172–186, 2006.
- 389 Applied Reservoir Technology Ltd.: The NMR Sandstone Rock Catalogue, Long Melford,
390 Suffolk, U.K., 1996.
- 391 Arnold, J., Clauser, C., Pechinig, R., Anferova, S., Anferov, V., and Blümich, B.: Porosity and
392 Permeability from Mobile NMR Core-Scanning, Petrophysics, 47, 306–314, 2006.
- 393 [Bird, N.R.A., Preston, A. R., Randall, E. W., Whalley, W.R. and Whitmore, A.P.:
394 Measurement of the size-distribution of water-filled pores at different matric potentials by
395 STRAFI-NMR relaxation-time measurements. European Journal of Soil Science. 56: 135-
396 143, 2005.](#)
- 397 Brownstein, K., and C. Tarr, C. (1979), Importance of classical diffusion in NMR studies of
398 water in biological cells, Phys. Rev. A, 19, 2446–2453, 1979.
- 399 Chen, S., Liaw, H. K., and Watson, A. T.: Measurements and analysis of fluid saturation-
400 dependent NMR relaxation and linebroadening in porous media, Magn. Reson. Imaging,
401 12(2), 201–202, 1994.
- 402 Coates, G. R., Xiao, L., and, Prammer, M. G.: NMR Logging Principles and Applications,
403 Halliburton Energy Services, Houston, TX, 234 pp., 1999.
- 404 [Costabel, S.: Nuclear magnetic resonance on laboratory and field scale for estimating
405 hydraulic parameters in the vadose zone, PhD thesis, Berlin University of Technology,
406 2011. \(opus4.kobv.de/opus4-tuberlin/files/3173/costabel_stephan.pdf\)](#)Costabel, S. and
407 Yaramanci, U.: Relative hydraulic conductivity in the vadose zone from magnetic
408 resonance sounding - Brooks-Corey parameterization of the capillary fringe, Geophysics,
409 76(3), G61–G71, doi:10.1190/1.3552688, 2011.

410 Costabel, S. and Yaramanci, U.: Estimation of water retention parameters from nuclear
 411 magnetic resonance relaxation time distributions, *Water Resour. Res.*, 49(4), 2068–2079,
 412 doi:10.1002/wrcr.20207, 2013.

413 Desbois, G., Urai, J. L., Kukla, P. A., Konstanty, J., and Baerle, C.: High-resolution 3D fabric
 414 and porosity model in a tight gas sandstone reservoir: A new approach to investigate
 415 microstructures from mm- to nm-scale combining argon beam cross-sectioning and SEM
 416 imaging, *J. Petrol. Sci. Eng.*, 78, 243–257, doi:10.1016/j.petrol.2011.06.004, 2011.

417 Dong, M. and Chatzis, I.: The imbibition and flow of a wetting liquid along the corners of a
 418 square capillary tube, *J. Colloid Interface Sci.*, 172, 278–288, 1995.

419 Dunn K. J., Bergman D. J., and LaTorraca G. A.: Nuclear Magnetic Resonance:
 420 Petrophysical and Logging Applications, Pergamon: Elsevier Science, Amsterdam, 2002.

421 Finjord, J., Hiorth, A., a Lad, U. H., and Skjaeveland, S. M.: NMR for equilateral triangular
 422 geometry under conditions of surface relaxivity - analytical and random walk solution,
 423 *Transport Porous Med.*, 69, 33–53. arXiv:cond-mat/0508412v2, 2006.

424 Fleury, M., Deflandre F., and Godefroy, S.: Validity of permeability prediction from NMR
 425 measurements, *CR. Acad. Sci. Series IIC – Chemistry*, 4, 869–872, doi:10.1016/S1387-
 426 1609(01)01343-3, 2001.

427 Ioannidis, M., Chatzis, I., Lemaire, C., and Perunarkilli, R.: Unsaturated hydraulic
 428 conductivity from nuclear magnetic resonance measurements, *Water Resour. Res.*, 42(7),
 429 [W07201](#), 6 pages, doi:10.1029/2006WR004955, 2006.

430 [Jaeger, F., Bowe, S., van As, H., and Schaumann, G. E. \(2009\). Evaluation of ¹H NMR](#)
 431 [relaxometry for the assessment of pore size distribution in soil samples. *European Journal of*](#)
 432 [Soil Science](#), 60:1052 – 1064.

433 Jia, P., Dong, M., and Dai, L.: Threshold pressure in arbitrary triangular tubes using RSG
 434 concept for all wetting conditions, *Colloid. Surface A*, 302, 88–95, 2007.

Comment [A1]: This is the article number

435 Kenyon, W.: Petrophysical principles of applications of NMR logging, Log Anal. 38(2), 21–
 436 43, 1997.

437 Kleinberg, R.L.: Utility of NMR T2 distributions, connection with capillary pressure, clay
 438 effect, and determination of the surface relaxivity parameter ρ_2 , Magn. Reson. Imaging,
 439 14(7), 761–767. doi: 10.1016/S0730-725X(96)00161-0, 1996.

440 Lenormand R., Zarcone C., Sarr, A.: A Mechanisms of the displacement of one fluid by
 441 another in a network of capillary ducts, J. Fluid Mech., 135, 337–353, 1983.

442 Liaw, H.-K., Kulkarni, R., Chen, S., and Watson, A.T.: Characterization of fluid distributions
 443 in porous media by NMR techniques, AIChE J., 42(2), 538–546, doi:
 444 10.1002/aic.690420223, 1996.

445 Marquardt, D. W.: An Algorithm for the Least-Squares Estimation of Nonlinear Parameters,
 446 Siam J. Appl. Math., 11(2), 431–441, 1963.

447 Mason, G. and Morrow, N. R.: Capillary behavior of a perfectly wetting liquid in irregular
 448 triangular tubes, J. Colloid. Interf. Sci., 141, 262–274, 1991.

449 Mayer, R. P., and Stowe, R. A.: Mercury porosimetry-breakthrough pressure for penetration
 450 between packed spheres, J. Colloid. Interf. Sci., 20, 893–911, 1965.

451 Mohnke, O.: Improved forward and inverse modelling of Surface NMR relaxation signals
 452 using multi-exponential decomposition, Ph.D. thesis, Technical University Berlin, [Berlin](#),
 453 2010.

454 Mohnke, O. and Klitzsch, N.: Microscale Simulations of NMR Relaxation in Porous Media
 455 Considering Internal Field Gradients, Vadose Zone J., 9, 846–857,
 456 doi:10.2136/vzj2009.0161, 2010.

457 [Øren, P. E., S. Bakke, and O. J. Arntzen, Extending predictive capabilities to network](#)
 458 [models, SPE Journal, 3, 324-336, 1998.](#)

459 Or, D. and Tuller, M.: Flow in unsaturated fractured porous media: Hydraulic conductivity of
 460 rough surfaces. Water Resour. Res., 36(5), 1165–1177, doi:10.1029/2000WR900020,
 461 2000.

462 Patzek, T. W., and D. B. Silin, Shape factor and hydraulic conductance in noncircular
 463 capillaries I. One-phase creeping flow, Journal of Colloid and Interface Science, 236,
 464 295-304, 2001.

465 Princen, H. M.: Capillary phenomena in assemblies of parallel cylinders I. Capillary rise
 466 between 2 cylinders, J. Colloid. Interf. Sci., 30, 69–75, 1969a.

467 Princen, H. M.: Capillary phenomena in assemblies of parallel cylinders II. Capillary rise in
 468 systems with more than 2 cylinders, J. Colloid. Interf. Sci., 30, 359–371, 1969b.

469 Princen, H. M.: Capillary phenomena in assemblies of parallel cylinders III. Liquid columns
 470 between horizontal parallel cylinders, J. Colloid. Interf. Sci., 34, 171–184, 1970.

471 Ransohoff, T. C., and Radke, C. J.: Laminar flow of a wetting liquid along the corners of a
 472 predominantly gas-occupied noncircular pore, J. Colloid Interface Sci., 121, 392–401,
 473 1987.

474 Seevers, D. O.: A nuclear magnetic method for determining the permeability of sandstones,
 475 Society of Professional Well Log Analysts, vol. 6, paper L, Houston, Texas, 1966.

476 Stingaciu, L. R.: Characterization of natural porous media by NMR and MRI techniques:
 477 High and low magnetic field studies for estimation of hydraulic properties, Ph.D. thesis,
 478 RWTH Aachen, URL: <http://darwin.bth.rwth-aachen.de/opus3/volltexte/2010/3392/>,
 479 2010a (accessed on 06/30/2014).

480 Stingaciu, L. R., Weihermüller, L., Haber-Pohlmeier, S., Stapf, S., Vereecken, H., and
 481 Pohlmeier, A.: Determination of pore size distribution and hydraulic properties using
 482 nuclear magnetic resonance relaxometry: A comparative study of laboratory methods.
 483 Water Resour. Res., 46, 1–11, doi:10.1029/2009WR008686, 2010b.

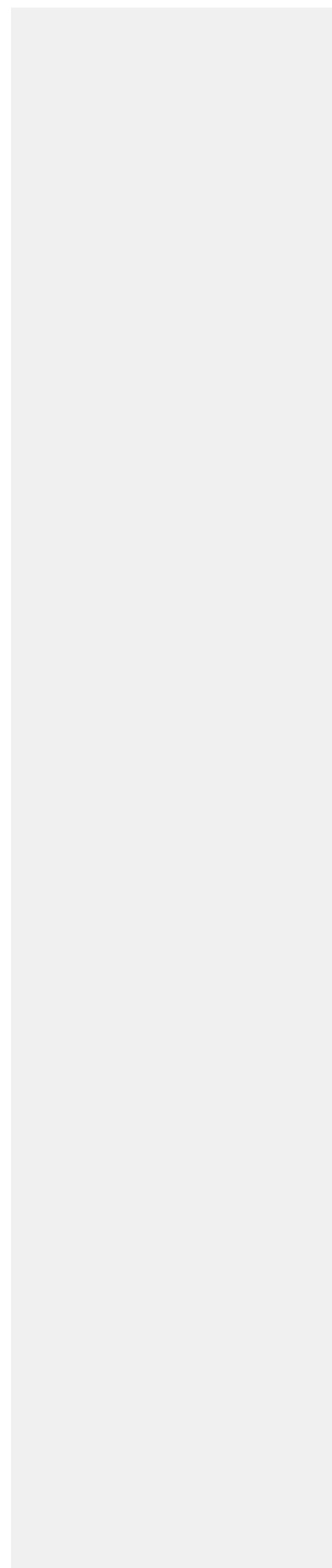
Formatted: Indent: Left: 0",
 Hanging: 0.25"

484 Talabi, O., AlSayari, S. Iglauer, I., and Blunt, J.: Pore-scale simulation of NMR response, J.
 485 Petrol. Sci. Eng., 67, 168–178, 2009.
 486 [Thern, H.: Examining the fluid film model in porous media by NMR rock catalogue data,](#)
 487 [Symposium of the Society of Core Analysts, Avignon, France, paper SCA2014-051.](#)
 488 Tokunaga, T. K. and Wan, J.: Water film flow along fracture surfaces of porous rock, Water
 489 Resour. Res., 33(6), 1287–1295, doi:10.1029/97WR00473, 1997.
 490 Toledo, P. G., Novy, R. A., Davis, H. T., and Scriven, L. E.: Hydraulic Conductivity of
 491 Porous Media at Low Water Content, Soil Sci. Soc. Am. J., 54, 673–679,
 492 10.2136/sssaj1990.03615995005400030007x, 1990.
 493 Torrey, H. C.: Bloch equations with diffusion terms, Phys. Rev., 104(3), 563–565,
 494 doi:10.1103/PhysRev.104.563, 1956.
 495 Tuller, M., Or, D., and Dudley, L.M.: Adsorption and capillary condensation in porous media
 496 - liquid retention and interfacial configurations in angular pores, Water Resour. Res.,
 497 35(7), 1949–1964, doi: 10.1029/1999WR900098, 1999.
 498 Tuller, M. and Or, D.: Hydraulic conductivity of variably saturated porous media: Film and
 499 corner flow in angular pore space, Water Resour. Res., 37(5), 1257–1276, [DOI:](#)
 500 [10.1029/2000WR900328](#)~~doi:10.1029/2000WR900~~, 2001.
 501

Formatted: Indent: Left: 0",
 Hanging: 0.25"

502 FIGURES

503



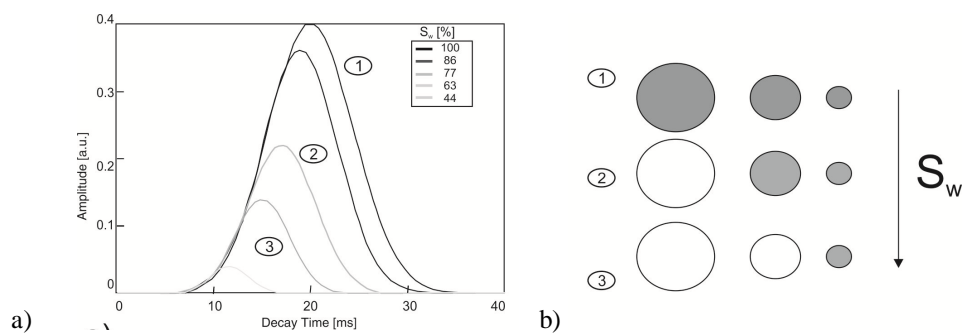


Figure 1. a) NMR decay time distributions at different water saturation levels for a classical cylindrical capillary pore distribution. b) Concept sketch of saturated (gray) and de-saturated capillaries, e.g., during drainage.

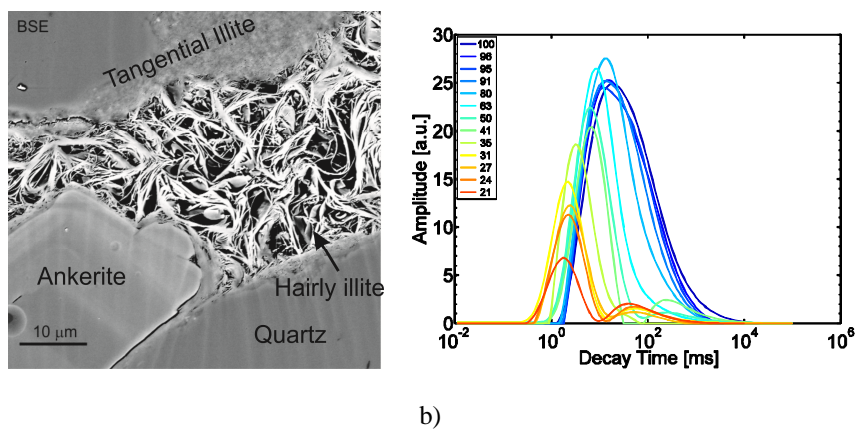


Figure 2. a) Complex pore structure of a Rotliegend tight gas sandstone. Pore spaces are filled with tangential and hairy illite and exhibit different pore types with elongated or slit-shaped, triangular, and multi-angular cross-sections. b) T_1 decay time distributions calculated from inverse Laplace transform performed on Rotliegend sandstone (porosity 13%, permeability 0.1 mD) at different water saturations ($S_w = 21\% - 100\%$).

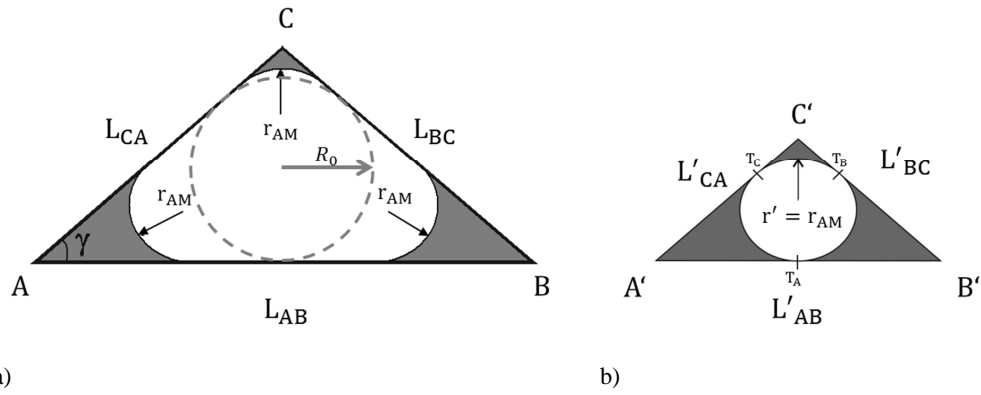
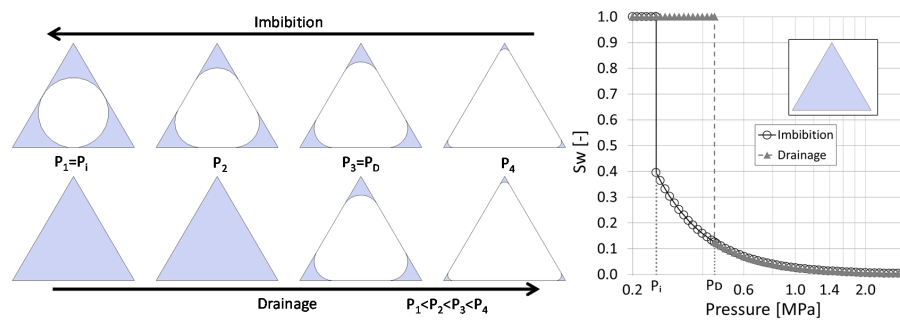


Figure 3. Cross-sections of a partially saturated triangular tube. Arc meniscus of radius r_{AM} separates invading non-wetting phase (white) from adsorbed wetting phase (gray). a) Original triangle ABC with side lengths L_{AB} , L_{BC} , L_{CA} , and radius R_0 of its inscribing circle. b) Reduced triangle $A'B'C'$ of similar geometry. The wetting phase resides in the three corners (gray) with $r' = r_{AM}$ being the radius of both the three interface arc menisci of ABC and of the inscribing circle of $A'B'C'$



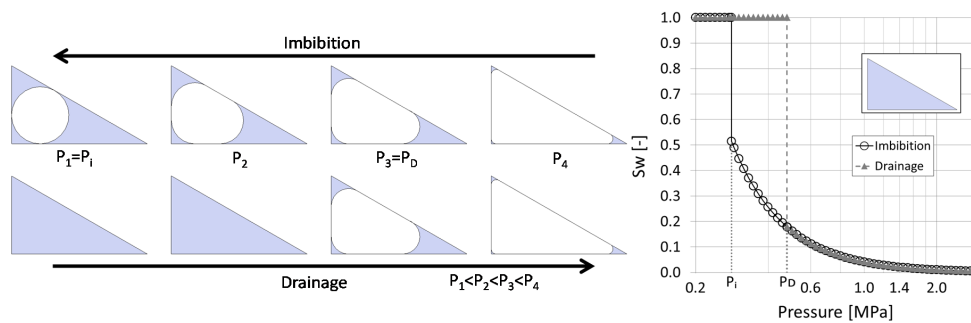
a)

b)

Figure 4. a) Modeled distribution of water (gray) and gas (white) phases in an equilateral triangular tube with a side length of $1 \mu\text{m}$ during imbibition (top) and drainage (bottom). b) Water saturation versus capillary pressure during imbibition (○) and drainage (▲).

508

509



a)

b)

Figure 5. a) Modeled distribution of water (gray) and gas (white) phases in a right-angled triangular capillary ($G = 0.39$) with side lengths $L = 1, 0.81, 0.58 \mu\text{m}$, and perimeter $P = 2.39 \mu\text{m}$ during imbibition (top) and drainage (bottom). b) Water saturation versus capillary pressure during imbibition (\circ) and drainage (\blacktriangle).

510

511

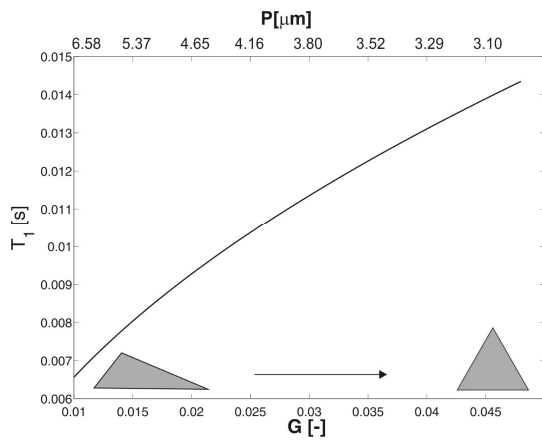


Figure 6. Longitudinal relaxation times T_1 of fully saturated triangular pores with constant cross-sectional area $A = 4.33 \cdot 10^{-13} \text{ m}^2$ versus shape factor $G = \frac{A}{p^2}$ and perimeter P . NMR parameters: $\rho_s = 10 \frac{\mu\text{m}}{\text{s}}$, $T_{1B} = 3 \text{ s}$.

512

513

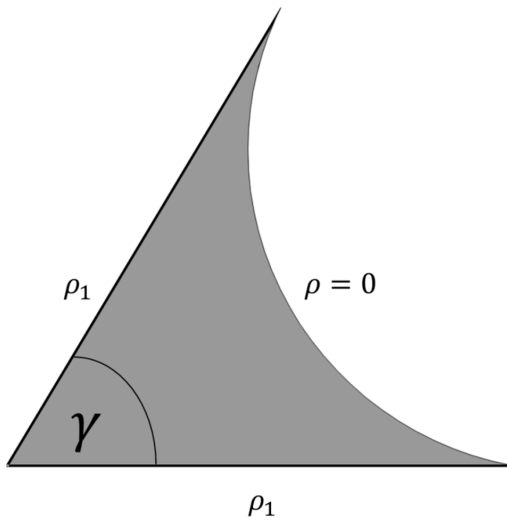


Figure 7. Saturated corner with active boundaries, i.e., $\rho_s = \rho_1 > 0$ at the corner's perimeter P_γ and a passive boundary at the air-water interface (meniscus), i.e., $\rho_s = \rho = 0$.

514

515

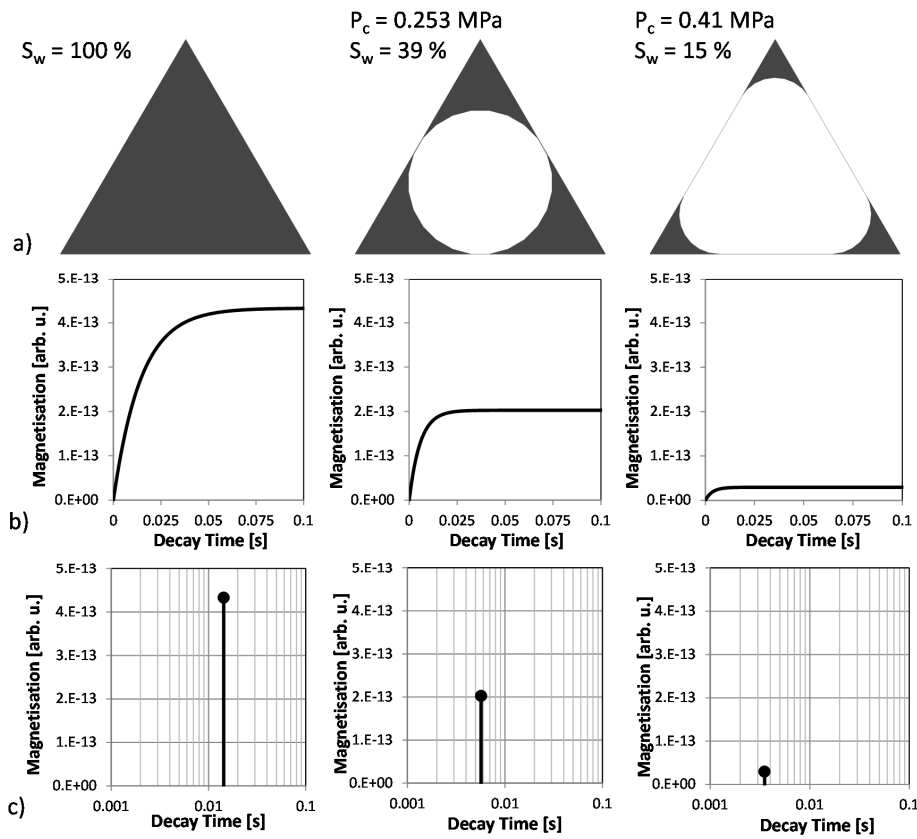


Figure 8. Water (black) and air (white) distributions within a triangular pore ($A_0 = 4.33 \cdot 10^{-13} \text{ m}^2$, $\rho_s = 10^{-5} \text{ m/s}$) at different capillary pressures for imbibition (a) with corresponding evolution of the (longitudinal) magnetization (b) and NMR T_1 relaxation times (c).

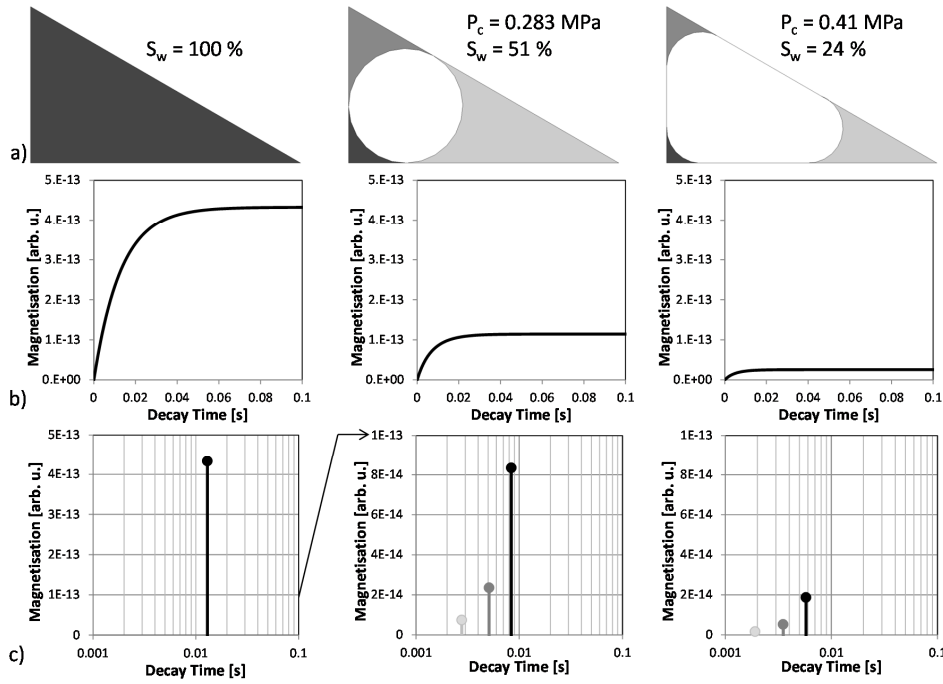


Figure 9. Water (black and grays) and air (white) distributions within a right-angled triangular pore ($A_0 = 4.33 \cdot 10^{-13} \text{ m}^2$, $\rho_s = 10^{-5} \text{ m s}^{-1}$) at different capillary pressures for imbibition (a) with corresponding evolution of the (longitudinal) magnetization (b) and NMR T_1 relaxation times (c).

518

519

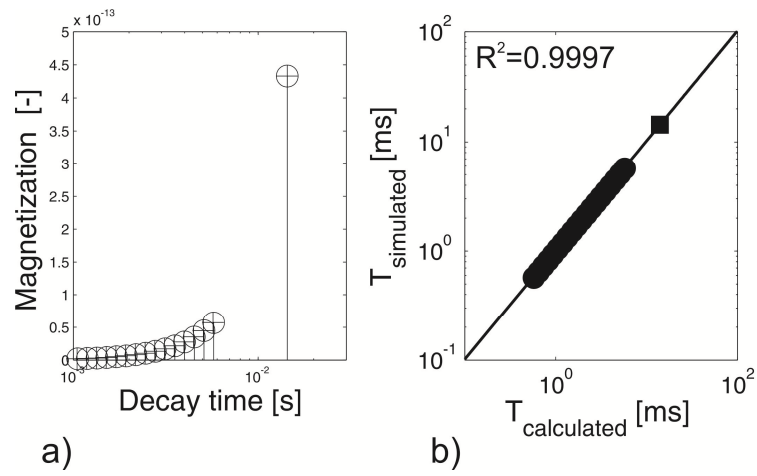


Figure 10. NMR response of an equilateral triangular capillary pore model (with a side length of $1\ \mu\text{m}$). a) Magnetization versus T_1 decay time data of numerical (\circ) and analytical solutions ($+$) for all applied pressure levels. b) Cross-plot of numerically simulated and analytically calculated longitudinal T_1 decay-times at partial (\bullet) and full water saturation (\blacksquare). A corresponding water saturation versus capillary pressure diagram is shown in Fig. 4.

520

521

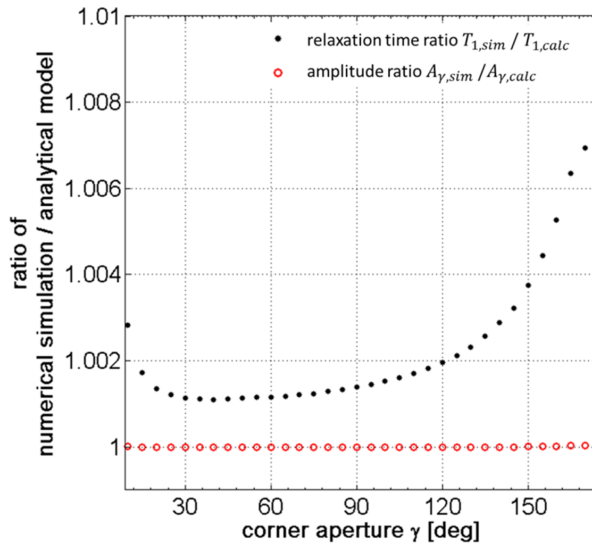
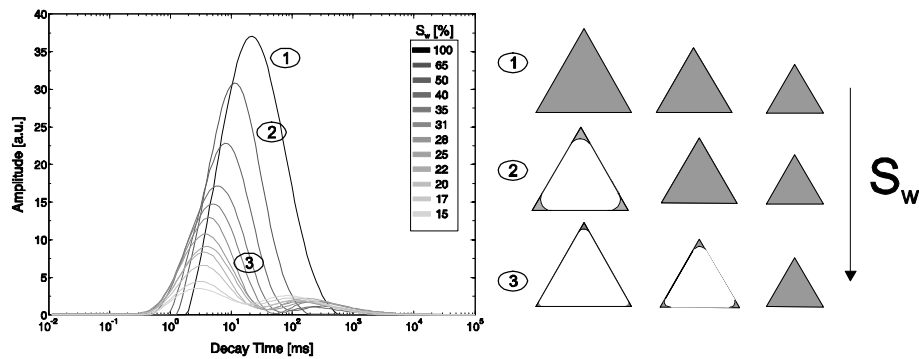


Figure 11. Comparison of analytical and calculated NMR relaxometry data originating from saturated pore corners (e.g. see Fig. 7) of varying apertures ($5^\circ < \gamma < 175^\circ$) and equal active surface-to-volume ratio $\frac{P_{\gamma i}}{A_{\gamma i}} = \text{const.}$ (NMR model parameters; $T_{1B} = 3\text{s}$, $D = 2.5 \cdot 10^{-9} \text{ m}^2 \text{ s}^{-1}$, $\rho_s = 10 \mu\text{m s}^{-1}$).

522

523



a)

b)

Figure 12. a) NMR decay time distributions at different water saturation levels for a pore distribution of equilateral triangles. b) Concept sketch of saturated (gray) and de-saturated triangular capillaries for increasing pressure levels (1), (2) and (3), e.g., during drainage.

524
525

Formatted: Indent: First line: 0.25",
Space After: 6 pt, Line spacing: 1.5
lines, Tab stops: 0.25", Left + 5.12",
Right + 6.2", Right

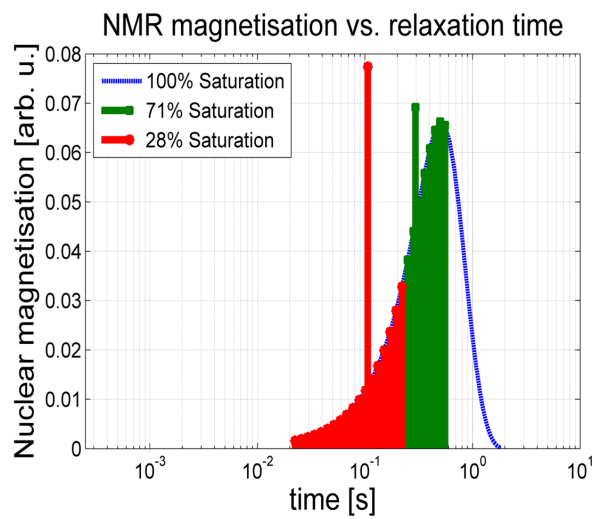


Figure 13: Relaxation components of fully (blue line) and partially de-saturated triangular pore size distribution. At a specific saturation level all pore corners with residual saturation exhibit the same NMR magnetization and relaxation behavior, thus superposing to a single fast relaxation component (e.g. red and green bars)

Formatted: Centered

Formatted Table

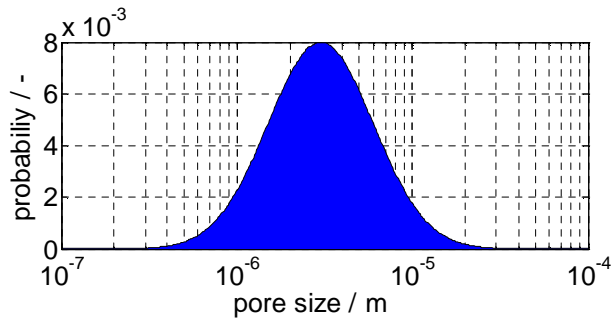


Figure 14. Pore-size distribution model (log-normal distribution: $\sigma = 0.3, \mu = 3 \mu\text{m}$) in analogy to that of the Rotliegend Sandstone shown in Fig. 2.

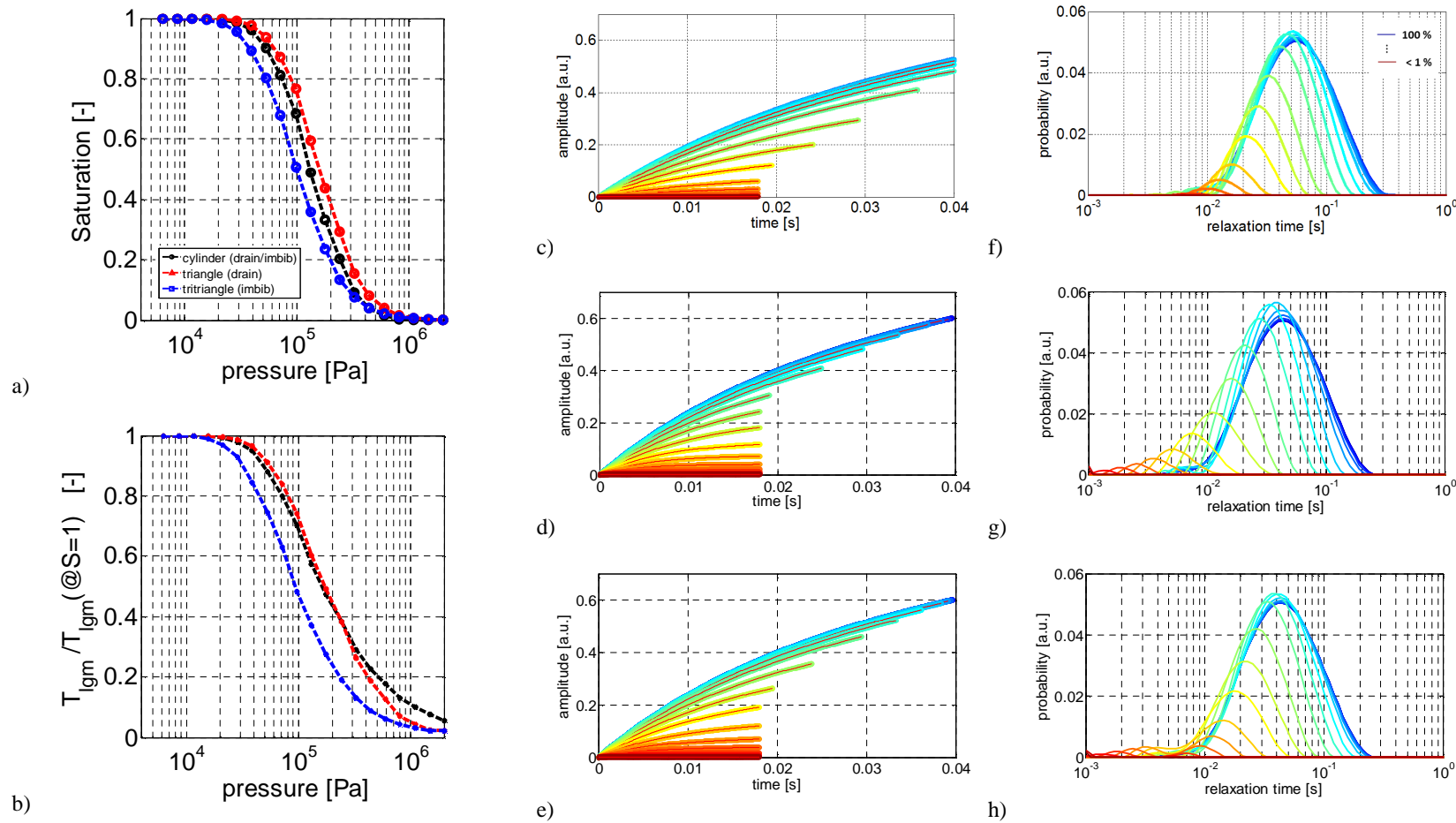


Figure 15: a) Modeled drainage and imbibition curves for circular and equilateral triangular capillary ensemble (cf Figure 14) and b) Corresponding normalized mean NMR T_1 relaxation times vs pressure curves. Modeled and fitted (red lines) NMR transient signals (longitudinal magnetization evolution) corresponding inverted NMR T_1 relaxation time distributions for 20 fully and partially saturated pore-size distributions ranging from < 1 % to 100 % saturation using circular (c, f) and equilateral triangular capillaries during imbibition (d, g) and drainage (e, h).

